OXFORD
SOT | Society of Toxicology
academic.oup.com/toxsci

Toxicological Sciences, 2026, **209(3)**, 1–15
https://doi.org/10.1093/toxsci/kfaf179
Advance Access Publication Date: December 24, 2025
Research Article

A human airway-on-a-chip microphysiological system for modeling chlorine gas toxicity

Sean V. Murphy[1,*], Shiny A.P. Rajan[1], Kevin Lindert[1], Tracey Young[1], Yan Jiao[1], Yu Zhou[1], Oula Khoury[1], Malcolm McSwain[1], Sivanandane Sittadjody[1], Zeeshan Hamid[3,6], Phillip W. Clapp[1], Timothy S. Leach[1], Timothy C. Orr[2], Douglas Shankle[1], Emily Whitaker[1], Khiry Sutton[1], Steven E. Albertson[1], Kristina Stumpf[1], Lysette Mutkus[1], Trang Simon[1], Gauri Kulkarni[1], Jeannie Chan[3,6], Jingyun Lee[3], Laura A. Cox[3,6], Ge Li[3], Charity Campbell[3,6], Michael Olivier[3,6], Sobha Puppala[3], Tony E. Reeves[1], Carl D. Langefeld[5], Hannah C. Ainsworth[5], Julie Ziegler[5], Amy Zinnia[5], Mohammad S. Khan[3], Frank C. Marini[1], Stephen J. Walker[1], Thomas D. Shupe[1], Alan Jacobson[1], Cristina M. Furdui[3], Andrew C. Bishop[3], Adam R. Hall[4], Michael C. Seeds[1], Kimberly D. Reeves[1], Anthony Atala[1]

[1]Wake Forest Institute for Regenerative Medicine, Wake Forest University School of Medicine, Medical Center Boulevard, Winston-Salem, NC 27157, United States
[2]Section of Gerontology and Geriatric Medicine, Department of Internal Medicine, Wake Forest University School of Medicine, Winston-Salem, NC 27157, United States
[3]Section on Molecular Medicine, Department of Internal Medicine, Wake Forest University School of Medicine, Winston-Salem, NC 27157, United States
[4]Department of Biomedical Engineering, Wake Forest University School of Medicine, Winston-Salem, NC 27157, United States
[5]Division of Public Health Sciences, Department of Biostatistical Sciences, Wake Forest University School of Medicine, Winston-Salem, NC 27157, United States
[6]Center for Precision Medicine, Wake Forest University School of Medicine, Winston-Salem, NC 27157, United States

*Corresponding author: Sean V. Murphy, Wake Forest Institute for Regenerative Medicine, Wake Forest University School of Medicine, 1 Medical Center Boulevard, Winston-Salem, NC 27157, United States. Email: sean.murphy@wfusm.edu

Abstract

There is a critical need to understand pathophysiological mechanisms involved in injury from acute chlorine gas (Cl_2) exposure. Limited information is available regarding the time course and mechanisms of injury after acute Cl_2 exposure due to a lack of human clinical data and limited fidelity of pre-clinical animal models. We designed and integrated a Cl_2 exposure platform to generate and deliver precise concentrations of Cl_2 to a microfluidic human airway-on-a-chip microphysiological system. Chemical, biological, structural, and functional airway-on-a-chip responses to Cl_2 exposure were characterized across multiple concentrations, exposure times, and post-exposure timepoints. Transcriptomics and metabolomics analyses delineated key molecular, cellular, and physiological pathways involved in the acute response to Cl_2 exposure. This work represents a significant advancement towards high-throughput, human-relevant characterization of pulmonary toxicants and medical countermeasure development, addressing critical gaps in toxicology modeling while reducing reliance on animal studies.

Keywords: in vitro models; pulmonary toxicity; new approach methodologies; chlorine gas; airway; microphysiological system, organ-on-a-chip

Human exposures to chlorine gas (Cl_2) are primarily caused by transportation accidents, misuse of chemicals, industrial exposures, or use as a chemical warfare agent (Jones et al. 2010; Govier and Coulson 2018). The implications of a significant release of Cl_2 in a high-density area could result in exposure of as many as 700,000 people (Scenario 8: Chemical attack—chlorine tank explosion 2004). Of the exposed population, 5% could receive potentially lethal exposures, 15% will require hospitalization, whereas the remainder would require treatment and release at the scene. Compounding these risks is the lack of effective medical countermeasures (MCMs) for Cl_2-induced lung injury (Huynh Tuong et al. 2019). Limited information is available regarding the dosimetry and time course of injury after acute Cl_2 exposure due to the unanticipated and uncontrolled nature of human exposure situations.

Preclinical animal models of acute Cl_2 exposure face significant limitations in safety, ethics, cost, and throughput that constrain their utility for establishing human-relevant pathophysiology and therapeutic indices (Wang et al. 2005; Batchinsky et al. 2006; Leustik et al. 2008; White and Martin 2010; Zarogiannis et al. 2011; Samal et al. 2012; Watkins et al. 2021; Baljinnyam et al. 2023; Clark et al. 2023; Gustafson et al. 2023; Liu et al. 2023; Matalon et al. 2024; Hemstrom et al. 2024). A single acute chlorine exposure study in rodents requires specialized containment facilities, trained personnel, and involves significant costs for animal acquisition, housing, and veterinary oversight. The logistical complexity and expense of such studies severely limit the throughput necessary for comprehensive dose-response characterization or therapeutic screening. Typical animal studies utilize sample sizes in the range of 3 to 10 animals per group (Leustik et al. 2008; Samal et al. 2012; Clark et al. 2023) to achieve statistical power, whereas airway-chip studies such as our own employ comparable sample sizes yet enable parallel testing of multiple exposure conditions with substantially reduced time, cost, and ethical burden while providing human-relevant cellular responses. Our recently developed 3D airway model (Leach et al. 2023), integrated into a microfluidic chip platform, hereby referred to as an airway-chip,

incorporates multicell type organization, biomimetic ECM hydrogel, and air–liquid interface capabilities, enabling tissue barrier measurements. These airway-chips demonstrate epithelial heterogeneity and function more representative of native tissue compared with traditional 2D monolayer cultures. Notably, airway-chips exhibit more accurate drug and xenobiotic metabolism responses (Skardal et al. 2020; Leach et al. 2023), making them particularly valuable for chemical exposure modeling.

Here, we describe the application and validation of airway-chips for modeling pulmonary toxicity resulting from exposure to Cl_2. We characterized chemical, biological, and functional airway-chip responses to Cl_2 exposure across multiple concentrations, exposure times, and measured at multiple post-exposure timepoints. Transcriptomics and metabolomics analyses delineated molecular, cellular, and physiological pathways involved in the acute response to Cl_2 exposure. This work represents a step toward the maturation of a 3D human airway-on-a-chip platform for the characterization of pulmonary toxins and informing the targeted screening of MCMs.

Materials and methods

Detailed methods can be found in the online supplementary material.

3D airway-on-a-chip model

3D *airway-on-a-chip* was fabricated as previously described (Leach et al. 2023), with modifications for integration into the microfluidic chip designed to maintain media flow and allow for accurate gas delivery to the epithelial air–liquid interface (Skardal et al. 2017; Rajan et al. 2020; Skardal et al. 2020). Following 6 d at liquid: liquid culture, apical media was removed, and airway-chips were exposed to air flow and maintained in an upright air-exposed culture for a minimum of 21 d. Human lung microvasculature endothelial cells were seeded on the basal surface of the airway-chips for a minimum of 7 d for experimental use.

Cl_2 exposure system

The Cl_2 exposure system provided calibrated Cl_2 mixtures to the airway-chips maintained at ±1 ppm (standard deviation of the mean) of the predefined Cl_2 concentration. The design included mass flow controllers (MFCs) that provided a calibrated flow of medical air (MA; 74% N_2, 21% O_2, 5% CO_2) either directly to airway-chips or to an electrochemical generator, where a controlled Cl_2 dose was introduced into the air stream before proceeding to the airway-chips. Six independent tissues can be exposed to Cl_2 gas, and an additional 6 tissues exposed simultaneously to MA as controls.

pH measurements

Measurements of airway-chip surface lavage fluid pH were performed using an Orion Versa Star Pro pH meter (Thermo Scientific) with up to 6 MI-410 Micro-Combination pH probes (Microelectrodes, Inc.) ($n = 5$–10). Measurement of circulating lower-chamber media or HBE was performed as above, in custom-made microfluidic flow cells in series downstream from exposed airway-chips. Measurements were recorded every 30 s for up to a 30 min exposure duration ($n = 3$).

Hypochlorous acid (HOCl) measurements

HOCl measures were performed using the BioTracker TP-HOCL1 Live Cell Dye (MilliporeSigma) ($n = 6$). Briefly, airway-chips were lavaged post-exposure with 20 µl of 250 µM HBS which was mixed 50:50 with 20 µM BioTracker TP-HOCL1 dye, incubated for 10 min and measured at Ex/Em = 375/500 nm. HOCl was quantified using a standard curve.

Mitochondrial superoxide

Mitochondrial superoxide was quantified using the Mitochondrial Superoxide Indicator (Red) Assay Kit (Abcam Cat# ab228567) ($n = 6$–9). Airway-chips incubated with the Superoxide Detection Agent for 10 min at 37 °C. Airway-chips were then washed 3× with PBS and incubated with the Live Cell Imaging Buffer with Hoechst 33342. Image capture and analysis were performed using the co-localization software module in the Nuance software (version 3.0.1.2).

Targeted detection of chlorotyrosine and chlorolipids

Chlorotyrosines (3-Cl-Tyr and 3,5-Cl_2-Tyr) were quantitated in airway-chips and basal circulatory media by liquid chromatography mass spectrometry (LC-MS/MS) following Cl_2 exposure as previously described (Crow et al. 2016) and detailed in Table S1 ($n = 6$). Chlorolipids (2-chloropalmitic acid and 2-chlorostearic acid) were quantitated in airway-chips by LC-MS/MS following Cl_2 exposure as previously described (Ford et al. 2016) and detailed in Table S2 ($n = 6$).

Live:dead viability assays

The LIVE/DEAD Viability/Cytotoxicity Kit (Thermo Fisher Scientific) was applied according to the manufacturer's instructions to quantify post-exposure airway-chip viability. Briefly, 2 µM Calcein AM and 8 µM of Ethidium Homodimer-1 were prepared in Hank's Balanced Salt Solution (HBSS) with $CaCl_2$ and $MgCl_2$. Image analysis was performed using the Olympus cellSens software, which quantified total cell number, total live (green) cells, and total dead (red) cells. Percentage viability was calculated as the number of live (green) cells divided by the total cell number (live + dead) ($n = 3$–6).

Transepithelial resistance (TEER)

TEER was adapted to the airway-chip platform by including electrodes into the chip design. Electrodes were inserted into access ports of the chips, allowing direct measurement of TEER between the apical and basal sides of the airway-chip. Sterile silver/silver chloride TEER probes were connected to an EVOM2 Epithelial Volt/Ohm Meter (World Precision Instruments) and introduced into the ports of the upper and lower chambers. Only airway-chips with baseline TEER values above 250 Ω/cm^2 were used for experimental studies. Once stable, TEER resistance data were measured and normalized to baseline values for each airway-chip ($n = 6$).

Caspase activation

The NucView 488 & MitoView 633 Apoptosis Assay Kit (Biotium) was used to profile apoptotic cells based on caspase 3/7 activity and changes in the mitochondrial membrane potential using fluorescence microscopy. Briefly, airway-chips were washed with HBSS and incubated for 15 min at 37 °C with staining solution containing 1× NucView 488 and 1× MitoView 633. Image analysis was performed using the co-localization software module in the Nuance software (version 3.0.1.2) and expressed as normalized values to mitochondrial membrane potential of airway-chips ($n = 6$).

Immunohistochemical staining

Immunofluorescence protocols were implemented for whole-mount and paraffin section staining. Whole mount samples

(VE-Cadherin, Phalloidin, Ac-TUB, CC10/SCGB1A1, MUC5AC) underwent fixation, permeabilization, and blocking before antibody incubation. Paraffin sections (p63) were deparaffinized and processed for antigen retrieval before antibody treatment. Quantification utilized Imaris software to measure RFU across multiple fields for VE-cadherin and F-actin ($n = 6$), p63/DAPI colocalization percentages, and volume ratios for CC10, α-tubulin, and MUC5AC positive staining ($n = 10$). A summary of primary and secondary antibodies used in this study is included in Table S3.

Transcriptomics

A total of 144 airway-chip tissues were exposed to either MA or 20 ppm Cl_2 with an exposure time of 30 min. Airway-chips were collected at 0-, 6-, 12-, and 24-h post-exposure. Exposures were performed across 3 batches of 48 airway-chips ($n = 6$ per timepoint for each exposure; $n = 18$ total per timepoint per exposure group). RNA was purified from lysed cells using QIAGEN's miRNeasy Micro Kit. Differential expression analysis using DESeq2 identified significantly altered genes at each timepoint. The top 400 associations (200 upregulated, 200 downregulated) were analyzed using STRING (Szklarczyk et al. 2023), Cytoscape (Bader and Hogue 2003), and REACTOME (Fabregat et al. 2017). Benjamini-Hochberg adjusted *P*-values (Benjamini and Hochberg 1995) and $\log_2$ fold changes were analyzed using IPA software (P_{adj} cutoff: 1.0×10^{-10}). Pathway significance was determined using Fisher's exact test ($P < 0.05$).

Metabolomics

A total of 144 airway-chips were exposed to either MA or 20 ppm Cl_2 for 30 min. Exposures were conducted across 3 independent experimental batches ($n = 3$ batches), each consisting of 48 airway-chips. Within each batch, airway-chips were divided into experimental conditions (MA or Cl_2) and sampled at 4 post-exposure timepoints (0, 6, 12, and 24 h). For metabolomic analysis, 6 airway-chips from the same condition and timepoint within a batch were pooled into a single tube to provide sufficient total protein for LC–MS/MS processing. Thus, each pooled sample represented the average metabolite profile of 6 airway-chips (pool-level $n = 1$), and each batch contributed one pooled sample per condition at each timepoint (batch-level $n = 1$ per condition/timepoint). Across the 3 independent batches, this yielded an effective $n = 3$ per condition at each timepoint for downstream statistical analysis (timepoint-level $n = 3$). Metabolomic analysis was performed according to the previously reported workflow (González-Ruiz et al. 2017) with minor modifications.

Statistical analysis

Each experimental dataset utilized a single donor set of cells, remaining consistent throughout the specific experiment, although multiple donors were utilized throughout the overall study due to the limited supply of primary human cells. For each experiment, each *n* represents a within-donor independent technical replicate airway-chip, defined as independently generated airway-chip tissues, derived from genetically identical donor tissue but fabricated, exposed, and analyzed independently. GraphPad Prism 10 was used for statistical analysis. Data are expressed as the mean ± SD from at least 3 independent experiments. Single factor comparison between the 2 groups using the unpaired 2-tailed Student's *t* test. One-way and 2-way ANOVA with post-hoc tests were used for comparisons of more than 2 groups. $P < 0.05$ was considered statistically significant. Detailed data and statistical analysis are included in the Supplementary Methods section.

Data availability

The transcriptomic datasets generated during this study are available in NCBI's Gene Expression Omnibus (GEO) and are accessible through GEO Series Accession Number GSE261463. Metabolomic data files are available from the corresponding author upon reasonable request. The source data underlying the figures are provided as Supplementary Data files. Additional datasets used during the current study are available from the corresponding author upon reasonable request.

Code availability

RNA-seq data processing was performed with Partek Flow software, differential expression analysis with DESeq2, and metabolomic data analysis with XCalibur Software. The analysis pipeline includes standard bioinformatics tools: Cutadapt (v3.4), STAR aligner (v2.7.9a), and DESeq2 (v1.34.0) packages implemented in R. No proprietary code was developed for this study.

Results

3D airway-on-a-chip

The airway-on-a-chip consists of a multi-cell type 3D tissue construct, combining primary human airway epithelial cells at an air–liquid interface, stromal cells in ECM hydrogel, and microvasculature endothelium in media (Fig. 1A). After 3 to 4 wk, airway-chips develop pseudostratified mucociliary differentiation resembling native tissue (Fig. 1B and C). Microfluidic chips enable controlled gas delivery and continuous media perfusion (Fig. 1D and E), with laminar flow in both air and fluid chambers (Fig. 1F). Calculated the Reynolds number (Re) for the flow within the microfluidic channels ranged from 0.33×10^{-7} to 3×10^{-7}, well below the laminar-turbulent transition threshold (Re > 3000).

Exposure parameters and system validation

The Cl_2 exposure system delivered metered MA to a modified electrochemical Cl_2 generator for room temperature (20 to 25 °C) gas blending (Fig. S2A). Total flow rate was 30 standard cubic centimeters per minute (sccm), distributed to 6 control airway-chips receiving MA only and 6 airway-chips receiving Cl_2 doses (5 sccm each) (Fig. S2B). Individual airway-chip flow rates maintained 1.15% average error over 30 min (Fig. S2C). System range was 3.75 to 375ppm Cl_2, validated at 5 ppm increments to 30 ppm for 30 min exposures (Fig. S2D and 2E).

Epithelial surface and circulating fluid pH

Cl_2 exposure experiments (10, 20, and 30 ppm) were conducted for 10, 20, and 30 min versus MA controls. Post-exposure pH measurements of airway-chip lavage (0.25 mM HEPES saline) revealed concentration- and time-dependent acidification (Fig. 2A). At 10 ppm, pH changes emerged at 30 min of exposure time. Exposure to 20 ppm Cl_2 demonstrated a broad pH change that was related to exposure duration, with a significant reduction in lavage pH following 20 min of Cl_2 exposure. The 30 ppm exposure demonstrated significant acidification by 10 min. Circulating fluid pH measurements showed minimal change (~0.5 pH units) in HEPES saline, with no decrease in culture media over 30 min at 30 ppm (Fig. 2B).

Hypochlorous acid (HOCl)

HOCl production was measured in the airway-chip surface lavage fluid (Fig. 2C) immediately following Cl_2 exposure as described above. With 10 ppm Cl_2 exposure, an increase in HOCl concentration compared with MA control was only detected

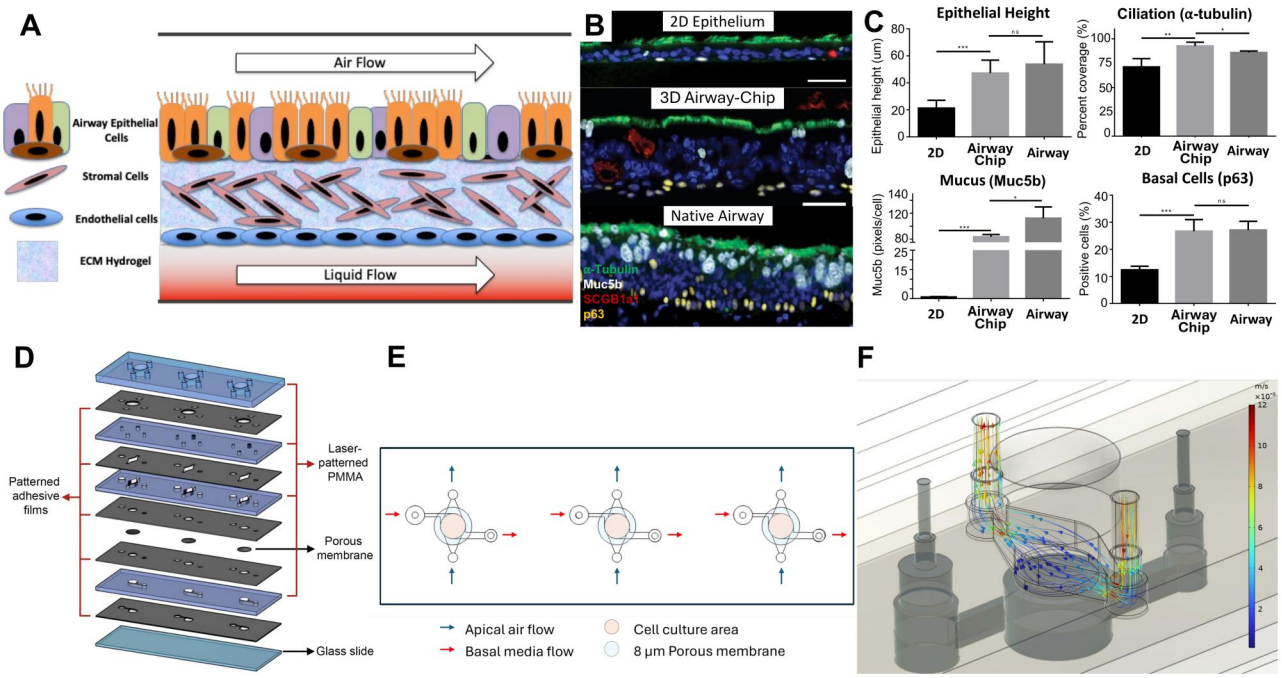

Fig. 1. Overview of the airway-on-a-chip microphysiological system. A) The airway-on-a-chip microphysiological system comprises a multi-cell-type planar 3D tissue construct with primary airway epithelial cells exposed to an air–liquid interface (ALI), a stromal layer comprising extracellular matrix (ECM) and lung stromal cells, and a microvasculature endothelium exposed to liquid media. B and C) Airway-chips possess an epithelial layer with increased pseudostratified mucociliary differentiation, epithelial cell height, ciliated cell numbers, mucin production, and epithelial heterogeneity more like native tissue than 2D monolayer cultures ($n = 11$, $^*P < 0.05$, $^{**}P < 0.01$, $^{***}P < 0.001$). D) Microfluidic chips are fabricated with a simple patterning technique of laser-cut polymethylmethacrylate (PMMA) layers stacked with adhesive film layers in a self-aligning manner. E) Airway-chip tissues are integrated into the microfluidic chips and maintained in microfluidic circuits comprising basal media flow and apical air flow. F) Circuits and flow rates are designed to support airway-chip function and physiologically relevant laminar flow at the gas interface. Native airway IHC image in panel B repurposed from graphical abstract in Leach et al. *Sci Rep*. 13:10137 (2023).

when exposed for 30 min. For both 20 and 30 ppm exposures, a significant Cl_2 concentration- and exposure time-dependent increase in HOCl was observed.

Mitochondrial superoxide production

Quantification of superoxide positive cells demonstrated a Cl_2 concentration- and time-effect on mitochondrial superoxide production as a proportion of airway-chip cells activated, derived by comparing superoxide- and Hoechst-positive pixel co-localization (Fig. 2D). A significant Cl_2 concentration- and exposure time-dependent increase in superoxide-positive airway-chip cells was detected following exposure to 20 and 30 ppm Cl_2.

Detection and quantitation of chlorinated proteins and lipids

3-Cl-Tyr and 3,5-di-Cl-Tyr have been proposed as biomarkers of respiratory tract exposure to Cl_2 (Sochaski et al. 2008; Nishio et al. 2021). For airway-chips exposed to 20 ppm Cl_2 for 30 min, the average concentration for 3-Cl-Tyr was 56.2 ± 14.0 ng/ml in airway-chip tissue samples and 92.0 ± 14.9 ng/ml in airway-chip media samples. For 3,5-di-Cl-Tyr, the average was 26.6 ± 6.1 ng/ml in airway-chip tissue samples and 63.6 ± 11.3 ng/ml in airway-chip media samples (Fig. 2E). Neither 3-Cl-Tyr nor 3,5-di-Cl-Tyr was detected in airway-chip tissue or media samples following control MA exposure only.

Chlorinated lipids, 2-chloropalmitic acid (2-Cl-PA) and 2-chlorostearic acid (2-Cl-SA), can also serve as indicators of Cl_2 exposure and may also have important downstream systemic effects (Marsche et al. 2004; Spickett 2007; Ford et al. 2016). For airway-chips exposed to 20 ppm Cl_2 for 30 min, the average concentration for 2-Cl-PA was 4.14 ± 0.12 ng/ml, and the average concentration for 2-Cl-SA was 3.45 ± 0.013 ng/ml in airway-chip tissue samples (Fig. 2F). 2-Cl-PA and 2-Cl-SA were not detected in the airway-chip media samples (data not shown) or MA-exposed airway-chips.

Post-exposure viability

Analysis of airway-chip viability following MA and Cl_2 exposures (10, 20, and 30 ppm for 10, 20, and 30 min) was assessed at 0-, 6-, 12-, and 24-h post-exposure. At 10 ppm Cl_2, 10 min exposures showed transient viability decrease with recovery by 24 h, whereas longer durations resulted in sustained decline to 56% to 60% viability (Fig. 3A). Exposure to 20 ppm Cl_2 demonstrated an exposure duration-dependent viability reduction, with immediate decrease to 66% to 75% and further decline to 45% to 55% by 24 h (Fig. 3B). At 30 ppm Cl_2, all exposure durations led to near-complete viability loss over 24 h (Fig. 3C). These findings established platform parameters for MCM intervention studies, with 20 ppm Cl_2 selected for subsequent mechanistic investigations based on its intermediate injury profile.

Trans-epithelial electrical resistance (TEER)

TEER measurements assessed airway-chip barrier function following MA (30 min) or Cl_2 exposures (10, 20, and 30 ppm for 10, 20, and 30 min) at baseline, 0-, 6-, 12-, and 24-h post-exposure. The lowest dose (10 ppm, 10 min) showed maximal TEER reduction at 6 h with complete recovery by 24 h (Fig. 3D). At 20 ppm, all exposures demonstrated 90% TEER reduction at 6 h, with minimal recovery observed only for 10- and 20 min exposures by 24 h (Fig. 3E). All 30 ppm exposures resulted in nearly

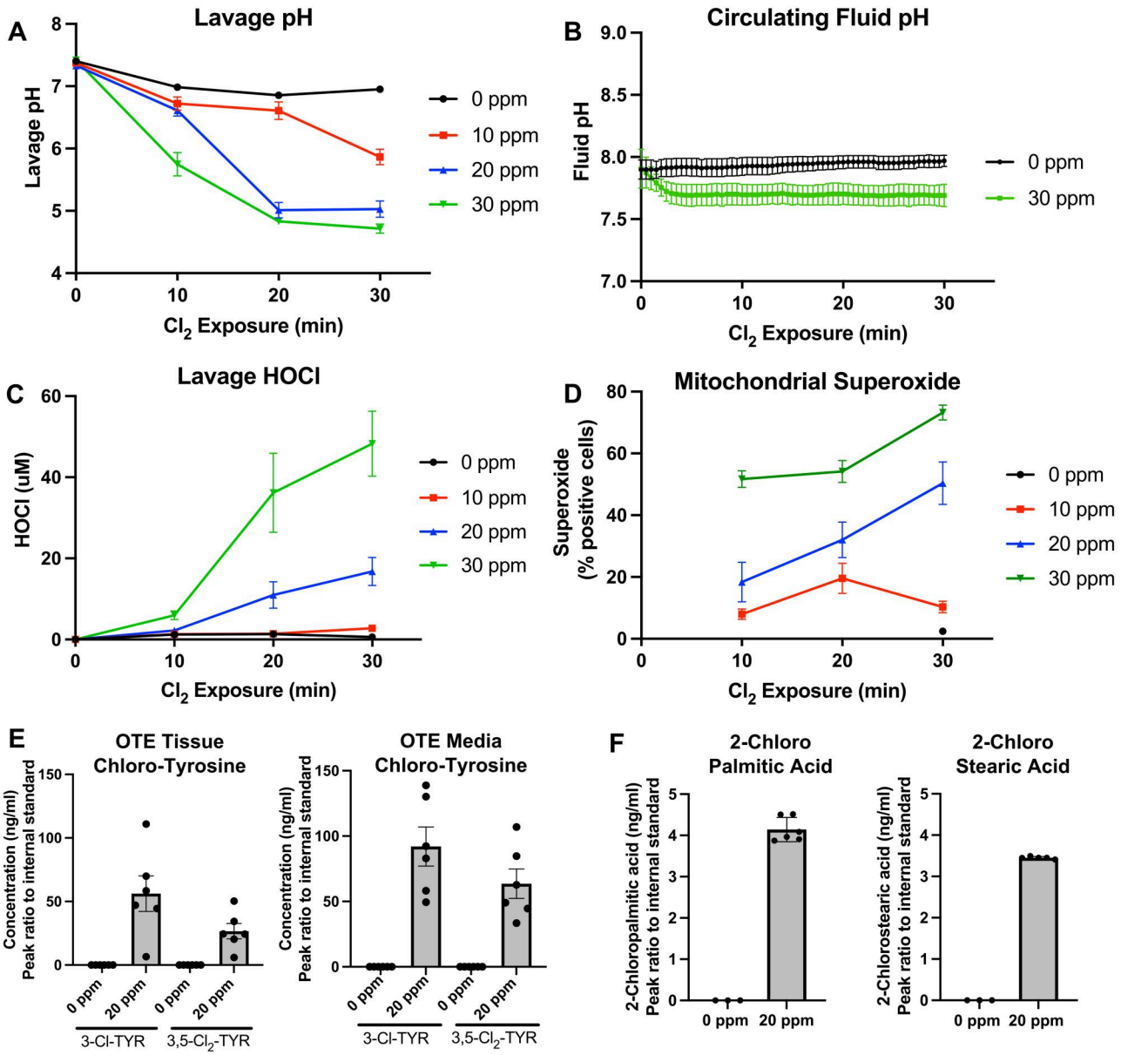

Fig. 2. Immediate biochemical impact of chlorine gas (Cl_2) exposure of the airway-on-a-chip microphysiological system. Cl_2 concentration and time experiments were performed using 10, 20, and 30 ppm Cl_2 vs medical air (MA – 0 ppm Cl_2) for exposure durations of 10, 20, and 30 min. A) Cl_2 exposure lowered the airway-chip epithelial surface lavage fluid pH in a concentration- and time-dependent manner, B) but only a minor decrease in the pH of circulating fluid (~0.5 pH units) was measured over the duration. C) A significant Cl_2 concentration- and exposure time-dependent increase in HOCl in the airway-chip lavage fluid was measured following exposure to 20 and 30 ppm Cl_2 for exposure times of 20 and 30 min at both concentrations. D) A significant Cl_2 concentration- and exposure time-dependent increase in superoxide positive cells was detected in airway-chips following exposure to 20 and 30 ppm Cl_2. E) Significant increases in the chlorinated amino acids, 3-chlorotyrosine (3-Cl-Tyr) and 3,5-dichlorotyrosine (3,5-Cl_2-Tyr), were found in airway-chips exposed to 20 ppm Cl_2 for 30 min. F) Significant increases in the chlorinated lipids, 2-chloropalmitic acid (2-Cl-PA) and 2-chlorostearic acid (2-Cl-SA), were also found in airway-chips exposed to 20 ppm Cl_2 for 30 min.

complete TEER reduction (approximately 100%) sustained through 24 h (Fig. 3F). MA exposure induced temporary TEER reduction at 6 h, suggesting airflow-mediated effects, with recovery by 12 h.

Epithelial and endothelial junctions

Airway-chip barrier analysis following exposure to MA or 20 ppm Cl_2 (30 min) utilized F-actin fluorescent probing for epithelial assessment and VE-cadherin IHC for endothelial evaluation. Epithelial barrier disruption, characterized by gap formation, was evident immediately post-Cl_2 exposure and persisted through 24 h (Fig. 3G). Endothelial barrier integrity, assessed at 0-, 24-, 48-, and 72-h post-exposure, showed significant disruption only at 72 h in Cl_2-exposed airway-chips (0- and 72-h shown in Fig. 3H).

Caspase activation

Apoptotic mechanisms were assessed in airway-chips exposed to 20 ppm Cl_2 (30 min). Significant caspase activation was observed at all timepoints (0-, 6-, 12-, and 24-h) post-Cl_2 exposure compared with MA controls (Fig. 3I). Post-exposure caspase levels stabilized

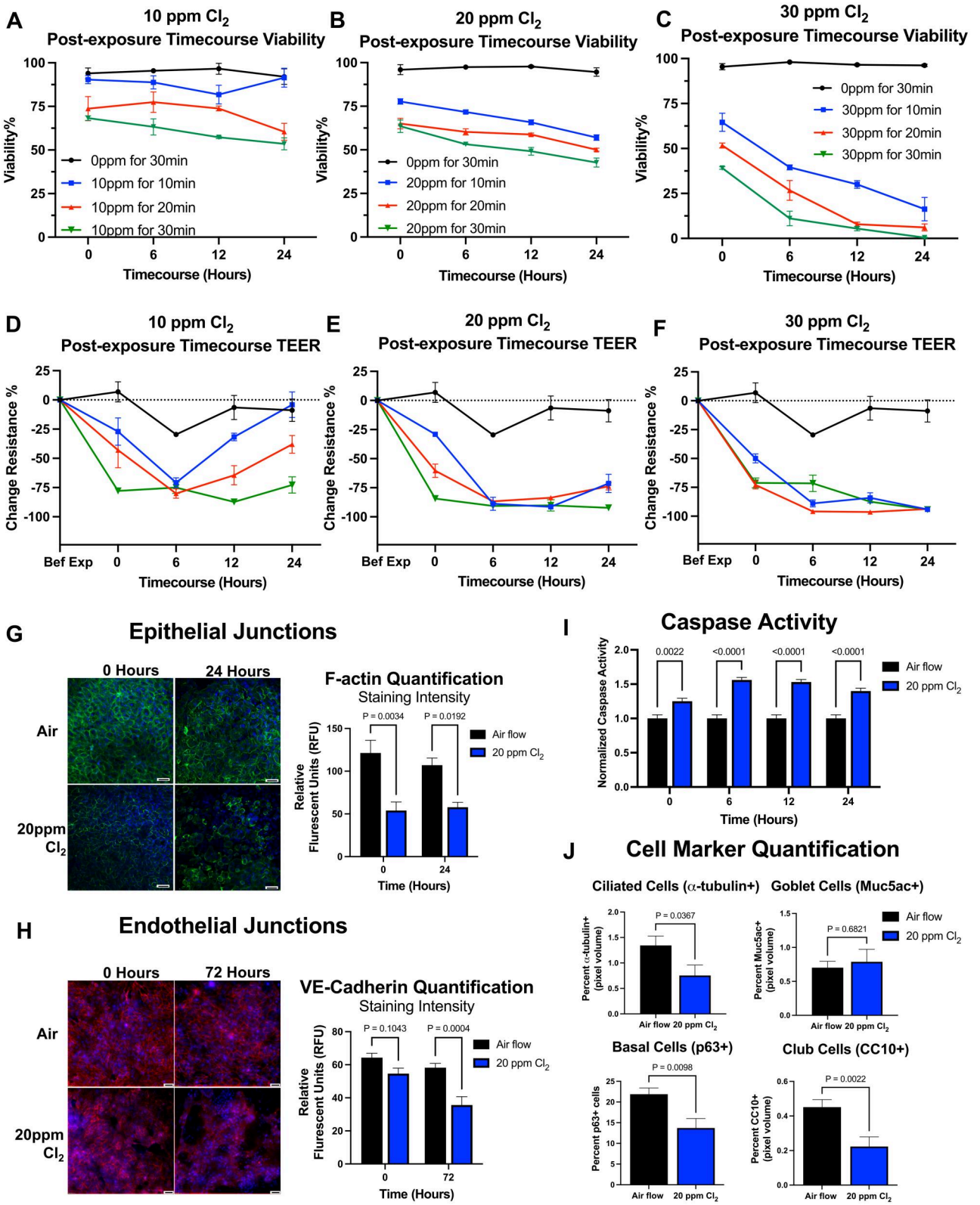

Fig. 3. Time course of the biological impact of chlorine gas (Cl_2) exposure of the airway-on-a-chip microphysiological system. Cl_2 concentration and time experiments were performed using 10, 20, and 30 ppm Cl_2 vs medical air (MA – 0 ppm Cl_2) controls for exposure durations of 10, 20, and 30 min. Airway-chip biological responses were evaluated immediately post-exposure (0-h) as well as 6-, 12-, 24- or 72-h post-exposure. A–C) Cl_2 exposure conditions were defined that encompass the entire range of viability outcomes that could be relevant for acute human exposures, with the lowest 10 ppm Cl_2 for 10 min exposure showing minimal airway-chip injury and full recovery, whereas 30 ppm Cl_2 exposure for 30 min resulted in an almost total loss of viability. D–F) Transepithelial electrical resistance (TEER) measurements of barrier function also showed recoverable function at 10 ppm Cl_2, progressing to a critical loss of barrier function at higher concentrations or exposure durations. G) Disruption to the airway-chip epithelial barrier was observed immediately after exposure to 20 ppm Cl_2 for 30 min through 24-h post-exposure. Scale bar = 50 μm. H) The airway-chip endothelial barrier was maintained immediately after exposure to 20 ppm Cl_2 for 30 min, but demonstrated measurable disruption at 72 h post-exposure. Scale bar = 50 μm. I) Relative levels of caspase through the post-exposure time course increased slightly after the 0-h timepoint and remained stable for the remaining timepoints. J) Quantification of several key airway-chip epithelial cell types showed a reduction in staining for α-tubulin, p63, and CC10 after exposure to 20 ppm Cl_2 for 30 min, whereas MUC5AC+ staining was unchanged compared with MA exposures.

after initial increase, indicating sustained apoptotic cell death, whereas mitochondrial membrane potential remained unchanged.

Epithelial cell phenotype

Airway-chip analysis of epithelial cell populations following exposure to MA or 20 ppm Cl_2 (30 min) was performed via IHC utilizing both confocal Z-stacks, and 2D maximum intensity projection (MIP) images at 24-h post-exposure (Fig. 3J and Fig S4). Quantification revealed significant reductions in α-tubulin+ ciliated cells, p63+ basal cells, and CC10+ secretory club cells in Cl_2-exposed airway-chips, whereas MUC5AC+ staining remained unchanged or slightly increased. These findings highlight the cellular susceptibility to Cl_2-induced toxicity, with preservation or potential increase of goblet cell populations and/or mucus production.

Transcriptomic analysis

RNA sequencing was performed to analyze gene expression changes in airway-chips following exposure to MA or 20 ppm Cl_2 (30 min duration), evaluating responses at 0-, 6-, 12-, and 24-h post-exposure. Each batch of transcriptomics data was reviewed for potential outliers, based on quality control checks, prior to analyses. Quality control checks included total read counts, principal component analyses (PCAs), and assessment of diversity indices using the exponentiated Shannon's index. A total of 8 outlier airway-chip samples were removed from analysis, with final sample numbers documented in Table S4. Temporal separation of expression profiles (Fig. 4A and Fig. S2) demonstrated immediate and sustained transcriptional responses to Cl_2 exposure. Comprehensive differential expression analysis results are detailed in Fig. 4B and Table S5 and raw datasets are available upon request.

'Cellular Responses to Stimuli' and 'Autophagy' were 2 reoccurring clusters (across exposure durations) identified by pathway analysis of the top 200 genes significantly upregulated and 200 genes downregulated. We selected 3 genes from each of these clusters to assess exposure effects across time as a linear test ($H_0 = \mu_1 < \mu_2 < \mu_3 < \mu_4$) and as a test of baseline effects ($H_0 = 3\mu_1 = \mu_2 + \mu_3 + \mu_4$). Results are shown in Table 1 and Fig. 4C. Transcriptomic analysis identified 106 genes meeting significance criteria ($P_{adj} < 1 \times 10^{-10}$) immediately following Cl_2 exposure, predominantly affecting EIF2 signaling pathways. Analysis across later timepoints (6, 12, and 24 h) revealed >200 significantly altered pathways, progressing from initial stress responses to immune pathway activation. This temporal progression culminated in enhanced cytokine and chemokine signaling networks by 12 to 24 h post-exposure, demonstrating a coordinated cellular response to Cl_2-induced injury.

Analysis of differentially expressed genes using IPA identified pathways significantly affected in airway-chips exposed to Cl_2 at each post-exposure timepoint. A subset of the top pathways identified as being activated and inhibited following Cl_2 exposure is shown in Table 2 and Table 3, and pathway categories are shown in Fig. 4D. Analysis revealed significant pathway inhibition across multiple timepoints post-Cl_2 exposure. AHR signaling was suppressed at 6 h, whereas xenobiotic metabolism and fatty acid β-oxidation were downregulated at 12 h. Oxidative phosphorylation emerged as the most consistently inhibited pathway across all timepoints (6 to 24 h), accompanied by sustained suppression of biosynthetic and nuclear receptor signaling pathways.

Metabolomics

Metabolomic profiling was performed using identical exposure conditions and timepoints as the RNA-seq analysis. PCA demonstrated clear separation between Cl_2-exposed and control airway-chips across timepoints (Fig. 5A and Fig. S3). Of 91 identified metabolites, 48 showed significant differences between Cl_2 and MA exposure in at least one timepoint. Metabolites meeting Bonferroni significance threshold ($P < 0.00055$) are detailed in Table S6, with increased levels shown in green and decreased levels in blue. Three metabolites (α-aminoadipate, L-phenylalanine, and inosine) exhibited persistent significant changes across all timepoints (Fig. 5B).

IPA analysis identified the top 15 affected pathways ($P < 0.001$) at each timepoint (Fig. 5C). Pathway activity was predominantly increased at later timepoints (12- and 24-h) compared with earlier timepoints (0- and 6-h), particularly in amino acid and amine compound transport/metabolism. Notably, the aminoacyl-tRNA charging pathway showed decreased activity at 12- and 24-h.

Analysis of biological processes (Fig. 5D) revealed an initial decreased cell survival post-exposure, returning to control levels by 24-h. Several processes increased across timepoints, including macromolecule metabolism, stress response, and molecular export. Ca^{2+} dynamics and metal ion quantities increased significantly by 12- and 24-h, whereas amino acid uptake and ROS formation decreased during these timepoints.

Discussion

There remains a critical gap in capabilities between single-cell monolayer cultures and the existing rodent and large animal studies. Our study aims to provide an advanced in vitro human primary cell airway-on-a-chip microphysiological system that better recapitulates the structure, composition, and function of human airway tissue and addresses the capability gap between existing pre-clinical models of airway exposures to Cl_2. Findings from this study are consistent with key known characteristics and physiological responses of airway tissue following exposure, including rapid chemical changes of the airway surface fluid (Bosse 1994), formation of chlorinated biomarkers of exposure (Robaszkiewicz et al. 2011; Ahmad et al. 2015; Ford et al. 2016), epithelial (Mo et al. 2015) and endothelial (Samal et al. 2010) injury, loss of barrier function (Menaouar et al. 1997; Zellner and Eyer 2020), and inflammatory signaling (Massa et al. 2014; Clark et al. 2023). We also provide characterization of changes in the transcriptome and metabolome that may help improve understanding of injury mechanisms and guide the discovery of targeted MCMs.

Cl_2 absorption into airway tissues leads to epithelial surface fluid acidification through hydrochloric acid and HOCl generation. Our model demonstrates this rapid acidification, showing concentration- and time-dependent effects on airway-chip lavage fluid pH and HOCl levels. Cl_2-induced airway damage occurs through oxidative mechanisms, with rapid formation of reactive oxygen and nitrogen species (Martin et al. 2003; Evans 2005; Leustik et al. 2008). HOCl and hypochlorite form reactive intermediates that modify aromatic amino acids, generating chlorotyrosine residues (Robaszkiewicz et al. 2011) and chloramine, previously identified in Cl_2-injury models (Ahmad et al. 2015). Chlorinated lipids form through direct Cl_2 reactions with plasmalogen vinyl ether bonds, producing species like 2-chloropalmitic acid and 2-chlorostearic acid (Ford et al. 2016). Our data confirms rapid production of chlorotyrosine and chlorolipids

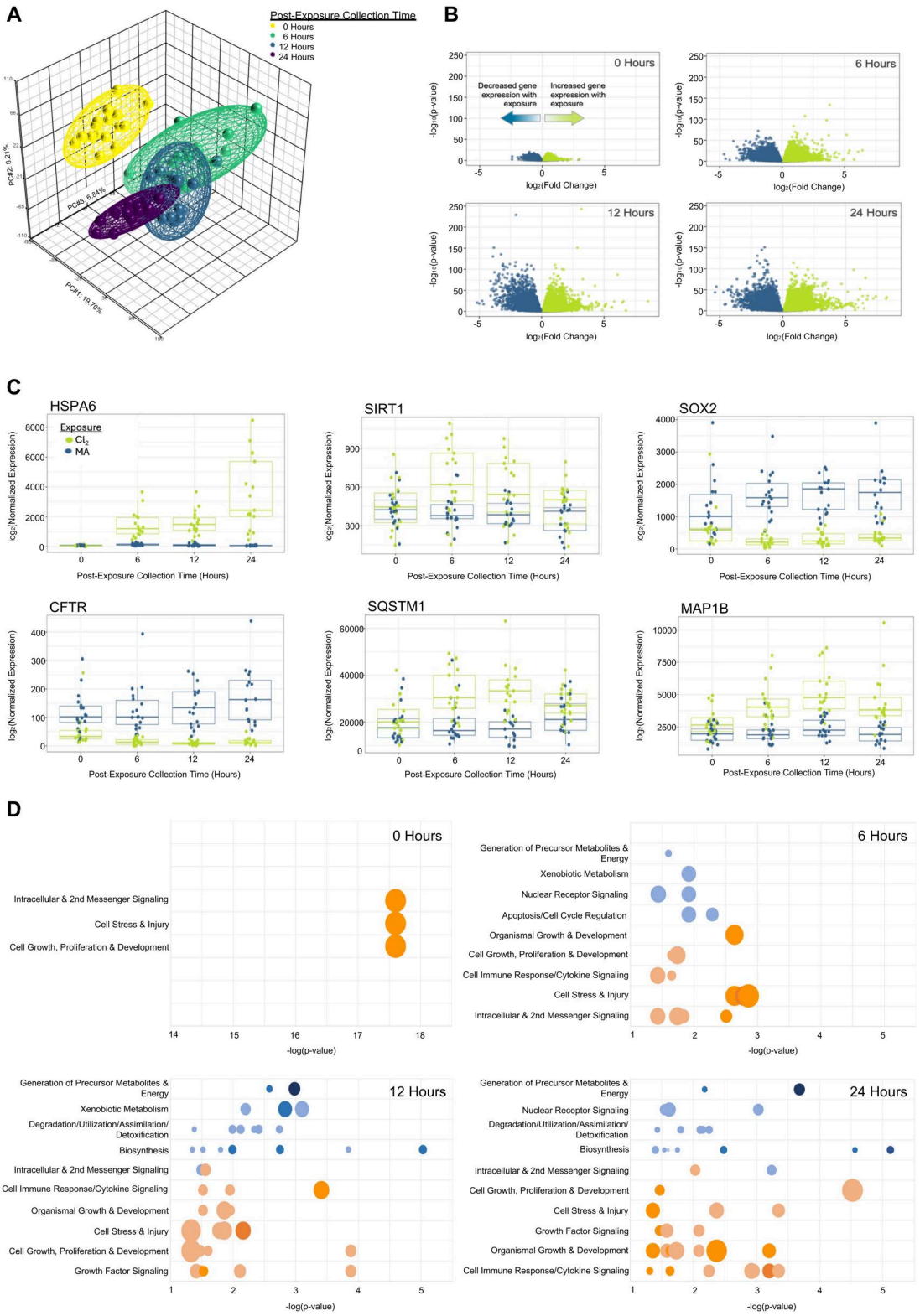

Fig. 4. Transcriptomic analysis of the airway-on-a-chip microphysiological system following chlorine gas (Cl_2) exposure. A) Principal component analysis (PCA) of gene expression profiles reveals partitioning of airway-chip tissue samples based on post-exposure collection time. Each point represents the gene expression profile of an individual airway-chip tissue, with point color corresponding to time after Cl_2 exposure. Variation attributed to the experimental batch was removed using the remove batch effect tool within Partek Genomics Suite to visualize the biological effects of Cl_2 exposure. B) Volcano plots summarizing differential expression by $\log_2$ fold change (LFC) on the X-axis and $-\log_{10}$(P-value) on the Y-axis indicate Cl_2-induced significant transcriptome changes across all timepoints. Data points with LFC > 0 exhibited increased expression with Cl_2 exposure, whereas LFC < 0 exhibited decreased expression. C) Three genes from "Cellular Response to Stimuli" and 3 genes from "Autophagy" MCODE clusters that exhibited significant expression changes by exposure. *HSPA6* shows increased expression with time (0 to 24 h); *SIRT1* shows increased expression at 6 h, decreasing to baseline by 24 h; *SQSTM1* and *MAP1B* show increased expression through 12 h, then decreasing at 24 h. *SOX2* and *CFTR* exhibit consistent reduction compared with medical air across time. Immediately post-exposure (0 h), 106 genes met significance criteria ($P_{adj} < 1 \times 10^{-10}$), predominantly involving EIF2 signaling. Analysis of 6, 12, and 24 h timepoints identified >200 significantly altered pathways, including cellular stress responses, intracellular signaling cascades, and inflammatory mediators. D) Categories of pathways significantly affected in airway-chips exposed to

Fig. 4. Continued
Cl_2 at each timepoint. Early responses showed suppression of AHR signaling, whereas intermediate timepoints demonstrated downregulation of xenobiotic metabolism and fatty acid β-oxidation. Oxidative phosphorylation was consistently inhibited across all timepoints (6 to 24 h). Pathways are grouped by category (*Y*-axis), with the negative log of Fisher's Exact test *P*-value shown (*X*-axis). Pathway bubbles are colored by z-score: ≥2 indicates activation (orange), ≤−2 indicates inhibition (blue). Bubble size correlates with gene overlap.

Table 1. Reoccurring gene clusters identified by pathway analysis.

Pathway	Gene	ENSEMBLID	Direction of effect with CE	*P*-value (global test) $H_0 = \mu_1 = \mu_2 = \mu_3 = \mu_4$	*P*-value (linear test) $H_0 = \mu_1 < \mu_2 < \mu_3 < \mu_4$	*P*-value (baseline test) $H_0 = 3\mu_1 = (\mu_2 + \mu_3 + \mu_4)$
Cellular responses to stimuli	HSPA6	ENSG00000173110.8	Increased expression	6.07E−32	1.40E−12	2.26E−17
Cellular responses to stimuli	SIRT1	ENSG00000096717.12	Increased expression	1.97E−39	2.59E−01	2.32E−02
Cellular responses to stimuli	SOX2	ENSG00000181449.4	Decreased expression	1.13E−38	9.94E−02	8.92E−01
Autophagy	CFTR	ENSG00000001626.16	Decreased expression	2.92E−36	7.78E−02	4.44E−04
Autophagy	SQSTM1	ENSG00000161011.20	Increased expression	2.78E−25	2.08E−05	1.11E−07
Autophagy	MAP1B	ENSG00000131711.15	Increased expression	2.95E−29	4.06E−05	9.35E−08

Analysis of selected genes from 2 MCODE-identified clusters based on transcriptomics data. We selected 3 genes from each of these clusters to assess exposure effects across time as a linear test ($H_0 = \mu_1 < \mu_2 < \mu_3 < \mu_4$) and as a test of baseline effects ($H_0 = 3\mu_1 = (\mu_2 + \mu_3 + \mu_4)$). Although a global comparison across timepoints ($H_0 = \mu_1 = \mu_2 = \mu_3 = \mu_4$) yielded highly significant *P*-values across all 6 genes, the "linear" and "baseline" tests reveal the variability of expression changes with exposure duration.

Table 2. Top activated pathways identified following Cl_2 exposure.

	0 h		6 h		12 h		24 h	
Canonical pathways	**z-score**	**−log(*P*-value)**	**z-score**	**−log(*P*-value)**	**z-score**	**−log(*P*-value)**	**z-score**	**−log(*P*-value)**
EIF2 signaling	2.65	17.60	0.89	—	0.78	—	1.06	—
NRF2-mediated oxidative stress response	—	—	3.27	2.79	3.27	2.16	0.52	1.15
G beta gamma signaling	—	—	3.00	0.31	2.75	0.57	2.06	1.30
Agrin interactions at neuromuscular junction	—	0.45	2.84	1.73	0.43	1.93	1.04	2.02
ERK5 signaling	—	—	2.68	2.51	2.18	0.50	2.45	1.02
Pulmonary fibrosis idiopathic signaling pathway	—	—	2.65	2.86	2.36	1.17	2.74	1.20
Autophagy	—	—	2.65	2.64	2.29	1.86	2.71	1.36
Ceramide signaling	—	—	2.40	2.29	1.13	2.05	0.67	3.40
Endothelin-1 signaling	—	—	2.40	1.43	2.56	2.61	1.95	2.62
Oncostatin M signaling	—	—	2.31	1.65	2.14	0.94	1.73	0.33
α-Adrenergic signaling	—	—	2.31	1.09	2.07	1.56	0.43	2.12
PI3K/AKT signaling	—	—	2.19	1.74	2.06	0.51	1.67	1.19
Role of NFAT in regulation of the immune response	—	—	2.19	1.43	0.91	2.10	1.09	1.08
Renin-angiotensin signaling	—	—	2.07	0.87	2.06	2.11	1.95	2.09
IL-8 signaling	—	—	0.78	2.70	2.58	3.41	2.39	2.92
ERBB4 signaling	—	—	1.60	1.20	2.52	1.53	1.53	1.73
Thrombopoietin signaling	—	—	1.81	1.43	2.40	1.60	0.82	1.96
VEGF family ligand-receptor interactions	—	—	1.34	2.08	2.34	3.88	1.77	3.33
Erythropoietin signaling pathway	—	—	1.23	0.63	2.34	1.41	0.14	2.17
Hepatic fibrosis signaling pathway	—	—	0.91	0.94	2.32	1.33	1.91	3.20
SPINK1 general cancer pathway	—	—	1.50	2.15	2.24	1.58	1.96	1.38
Chemokine signaling	—	—	1.41	1.85	2.20	1.95	2.50	1.63
Pulmonary healing signaling pathway	—	—	0.97	1.89	2.18	1.78	1.97	3.34
NF-κB signaling	—	—	1.46	1.03	2.11	1.03	2.84	3.20
STAT3 pathway	—	—	1.79	0.87	2.06	1.41	0.93	4.38
Thrombin signaling	—	—	0.69	2.55	2.02	1.97	1.84	3.30
IL-17 signaling	—	—	0.51	3.38	0.71	3.51	2.77	3.20
IL-6 signaling	—	—	0.66	0.67	0.90	0.57	2.41	2.25
HMGB1 signaling	—	—	0.82	1.15	1.72	1.16	2.36	3.35
FGF signaling	—	—	0.26	1.10	0.82	1.78	2.35	1.46
FAK signaling	—	0.29	0.33	2.82	1.50	3.84	2.32	4.52
Regulation of the epithelial mesenchymal transition by growth factors pathway	—	—	1.30	2.12	1.55	3.88	2.18	1.57
Endocannabinoid developing neuron pathway	—	—	1.04	1.67	1.51	1.06	2.14	2.09
Wound healing signaling pathway	—	—	0.65	0.96	−0.28	0.33	2.12	2.37
CXCR4 signaling	—	—	0.96	1.41	1.98	2.29	2.02	2.95
Synaptogenesis signaling pathway	—	—	0.73	1.47	1.00	0.81	2.01	1.73

Most significant pathways with predicted activation in airway-chip tissues immediately after chlorine gas (Cl_2) exposure and at 6-, 12-, and 24-h post-exposure. The significance value (*P*-value of overlap) for each pathway was calculated using the right-tailed Fisher's Exact test. The calculated −log(*P*-value) is shown for each pathway; −log(*P*-values) ≥ 1.30 indicated significance (*P*-value ≤ 0.05). Overall activation/inhibition states of pathways were predicted based on a z-score algorithm; z-scores ≥ 2 are considered significant predictions of activation.

Table 3. Top inhibited pathways identified following Cl_2 exposure.

	0 h		6 h		12 h		24 h	
Canonical pathways	**z-score**	**−log(P-value)**	**z-score**	**−log(P-value)**	**z-score**	**−log(P-value)**	**z-score**	**−log(P-value)**
Aryl hydrocarbon receptor signaling	—	0.63	−2.00	1.92	−1.04	1.89	0.21	1.15
Oxidative phosphorylation	—	—	−4.24	0.74	−5.92	2.98	−5.70	3.68
TCA Cycle II (eukaryotic)	—	—	−2.65	1.60	−3.32	2.58	−3.32	2.18
PPARα/RXRα activation	—	—	−2.27	1.44	−2.14	1.04	−2.83	1.62
Gluconeogenesis I	—	—	−2.00	0.53	−2.12	1.35	−2.12	1.10
Superpathway of cholesterol biosynthesis	—	—	—	—	−3.50	5.03	−4.12	5.12
Xenobiotic metabolism signaling pathways	—	1.11	−1.35	0.72	−3.22	2.83	−1.94	1.83
Stearate biosynthesis I (animals)	—	—	−1.89	0.58	−3.05	1.99	−2.14	1.40
Estrogen biosynthesis	—	—	−1.51	1.79	−3.00	2.75	−3.15	2.48
Valine degradation I	—	—	—	0.38	−2.53	2.34	−2.12	1.07
Nicotine degradation II	—	—	−0.71	0.60	−2.50	1.99	−3.00	1.42
Fatty acid β-oxidation I	—	0.77	—	—	−2.50	2.74	−1.73	1.80
Mevalonate pathway I	—	—	—	0.22	−2.45	1.80	−2.45	1.54
Apelin adipocyte signaling pathway	—	—	−1.27	0.38	−2.40	1.49	−2.41	3.24
Ethanol degradation II	—	0.82	−1.00	0.27	−2.33	0.98	−2.11	1.43
Superpathway of melatonin degradation	—	—	−1.00	0.76	−2.18	2.12	−2.52	2.25
Acetone degradation I (to methylglyoxal)	—	—	−0.71	1.74	−2.11	2.74	−2.33	1.04
Methylglyoxal degradation III	—	—	—	—	−2.00	1.38	−2.00	0.63
PPAR signaling	—	—	−1.79	0.87	−1.00	0.34	−2.54	1.55
Serotonin degradation	—	0.60	−1.34	—	−1.94	0.77	−2.52	2.11
LXR/RXR activation	—	—	0.58	0.34	−1.53	1.70	−2.41	3.03
Zymosterol biosynthesis	—	—	—	0.23	−1.34	2.97	−2.00	1.60

Most significant pathways with predicted inhibition in airway-chip samples immediately after chlorine gas (Cl_2) exposure and at 6-, 12-, and 24-h post-exposure. The significance value (*P*-value of overlap) for each pathway was calculated using the right-tailed Fisher's Exact test. The calculated −log(*P*-value) is shown for each pathway; −log(*P*-values) ≥ 1.30 indicated significance (*P*-value ≤ 0.05). Overall activation/inhibition states of pathways were predicted based on a z-score algorithm; z-scores ≥ 2 are considered significant predictions of activation, and z-scores ≤ −2 are considered significant predictions of inhibition.

following Cl_2 exposure. These modifications serve as reliable biomarkers of Cl_2-exposure (Crow et al. 2016; de Bruin-Hoegée et al. 2022; Boles et al. 2024), distinguishing from other inflammatory diseases. Our findings validate previous exposure studies while providing a relevant human in vitro model for future clinical correlations.

Clinical outcomes of Cl_2-induced airway injury range from epithelial desquamation at low concentrations to acute lung injury, pulmonary edema, and respiratory failure at high concentrations (Das and Blanc 1993; Lemiere et al. 1997; Van Sickle et al. 2009). Our airway-on-a-chip microphysiological system demonstrated concentration-dependent responses: low-concentration exposures showed self-recovery within 24 h, whereas high concentrations caused rapid epithelial desquamation and critical loss of basal cells, leading to total lethality. At intermediate concentrations (20 ppm), we observed a linear decline in viability with potential for stabilization through intervention. Post-exposure analysis revealed significant reductions in ciliated, club, and basal cells, despite the predicted protection of basal cells within the pseudostratified layer. The maintained or slightly increased levels of MUC5AC staining could be interpreted as either the preservation of the goblet cell populations or potential mucus hypersecretion, as staining did not distinguish between intracellular and extracellular mucins. Exposure immediately compromised epithelial cytoskeleton integrity, with 50% junction loss persisting to 24 h. In contrast, endothelial junction disruption emerged at 72 h, supporting secondary endothelial dysfunction following epithelial oxidative injury. Previous studies demonstrate Cl_2 exposure disrupts vascular NO homeostasis (Samal et al. 2010; Honavar et al. 2011), potentially mediated by chloro-lipids affecting lung permeability and eNOS-dependent vasodilation (Ford et al. 2016). We anticipate that our model is well-suited for the examination of these mechanisms to support ongoing efforts in animal studies.

Transcriptome analysis of airway-chips following Cl_2 exposure revealed significant gene expression alterations across multiple timepoints. Immediately post-exposure, we observed significant upregulation of the EIF2 signaling pathway, indicating activation of the integrated stress response (Costa-Mattioli and Walter 2020). At 6- and 12-h post-exposure, our findings align with Clark et al. (2023), who described this as a "crisis" phase in murine models, characterized by upregulation of oxidative stress, protein degradation, and apoptosis pathways. We similarly observed the highest predicted activation of NRF2-mediated oxidative stress response (Elfsmark et al. 2018), along with upregulation of specific stress-response genes (*SNAI1*, *HSPA1A*, *HSPA1B*, *NAA16*, *HSPH1*). Both studies demonstrated significant downregulation of keratins and genes involved in epithelial barrier integrity during this phase. By 24 h, our data again paralleled Clark et al.'s "repair" phase, showing reversed transcriptional patterns with upregulation of keratins, *RPTN*, and cytoskeletal genes. Additionally, both models exhibited increased expression of multiple *Wnt* molecules linked to lung fibrosis, including *WNT2B*, *WNT3*, *WNT4*, *WNT5A*, *WNT7A*, *WNT7B*, and *WNT10A*.

Metabolomic analysis of Cl_2-exposed airway-chips revealed significant pathway alterations. We observed immediate ROS formation increase, consistent with anticipated HOCl generation (Evans 2005; Leustik et al. 2008). Supporting previous findings by Carlisle et al. (2016) showing disrupted cell bioenergetics, our analysis demonstrated early changes in transmembrane potential and a 5-fold increase in succinate, suggesting electron transport chain dysfunction. Similar to Ahmad et al.'s (2015) observations of impaired SERCA activity in cardiomyocytes, we found significant alterations in Ca^{2+} quantity and mobilization, noteworthy given Ca^{2+} dysregulation's role in airway pathologies (Amrani and Panettieri 2002; Philippe et al. 2015). These changes likely contribute to the observed "crisis" phase of epithelial dysfunction and oxidative stress. By 12 h post-exposure, metabolic profiles shifted

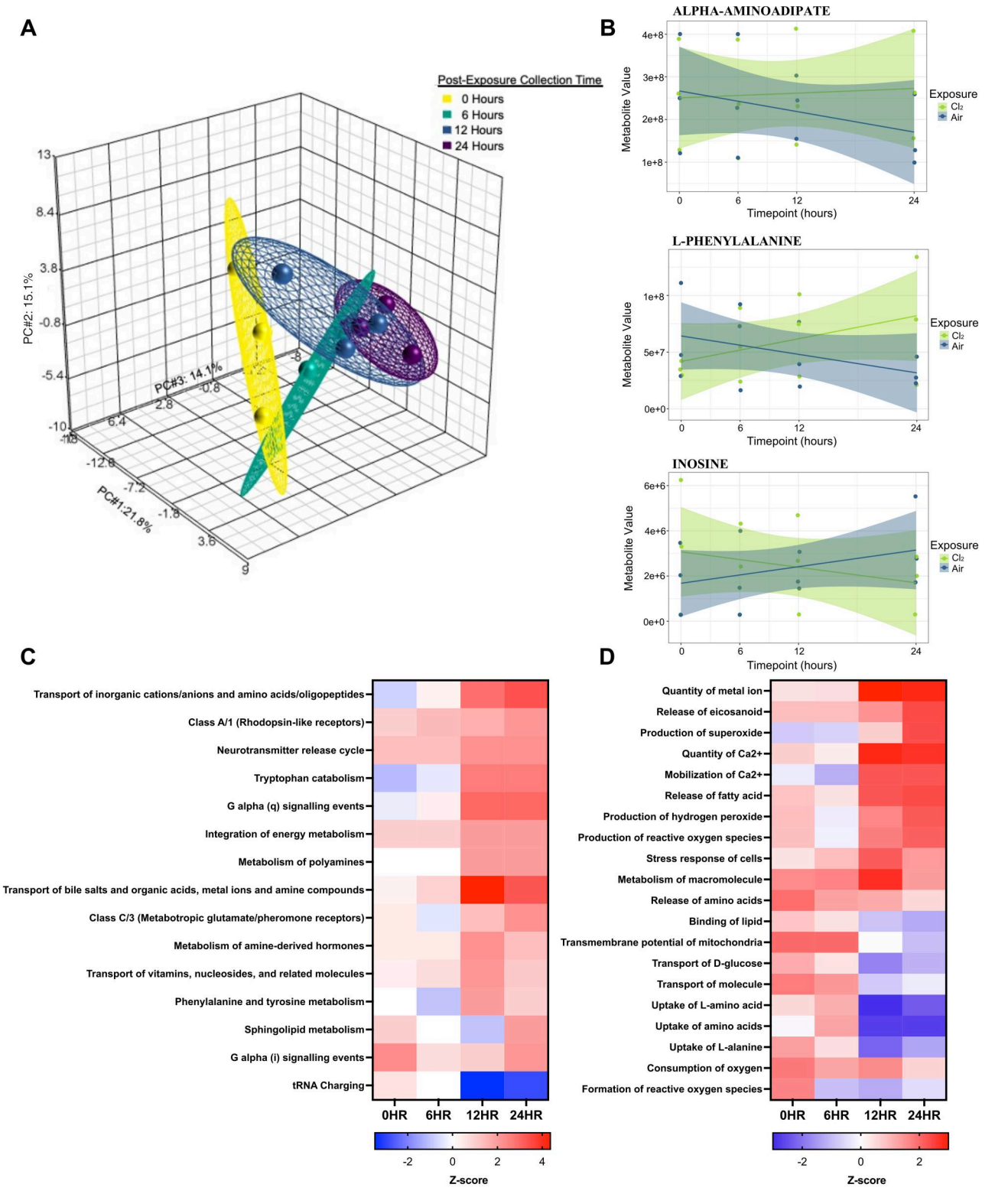

Fig. 5. Metabolomic analysis of the airway-on-a-chip microphysiological system following chlorine gas (Cl_2) exposure. A) PCA of metabolite profiles reveals partitioning of airway-chip tissue samples based on post-exposure collection time. Each point on the PCA represents the metabolomic profile of an individual airway-chip tissue. Point color corresponds to the time after Cl_2 exposure at which the tissue was collected. Variation attributed to the experimental batch was removed from metabolite data using the Remove Batch Effect tool within Partek Genomics Suite to visualize the biological effects of Cl_2 exposure. B) The top 3 identified metabolites (alpha-aminoadipate, L-phenylalanine, and inosine) showed a significant change following Cl_2 exposure that persisted over each of the post-exposure analysis timepoints. C) Ingenuity pathway analysis (IPA) top 15 relevant pathways based on log_2 fold change (LFC) of metabolites for each timepoint ($P < 0.001$). D) IPA top 10 relevant upregulated and downregulated cell processes based on fold change of metabolites over time ($P < 0.001$).

toward macromolecule synthesis and amino acid metabolism, supporting Clark et al.'s "repair" phase description. We observed significant increases in α-aminoadipate and L-phenylalanine, metabolites previously associated with ARDS (Viswan et al. 2017; Xu et al. 2020; Tang et al. 2023). These changes may reflect protein degradation and altered bioenergetics (Tojo et al. 2018), potential therapeutic targets for mitigating Cl_2-induced injury consequences (Batchinsky et al. 2006; White and Martin 2010).

Multiple strategies have emerged to address the physiological limitations of conventional 2D airway epithelial monocultures, including microfluidic airway-on-chip platforms (Benam et al. 2016; Humayun et al. 2018; Si et al. 2021), precision-cut lung slices (Liu et al. 2019; Alsafadi et al. 2020), and airway explants (Hirst 1996; Blume and Davies 2013). Our prior studies demonstrated that complex tissue-engineered 3D co-culture airway models can achieve more physiologically accurate cellular phenotypes and tissue architecture compared with 2D airway epithelial monocultures (Leach et al. 2023). Each of these approaches presents specific advantages and limitations regarding tissue complexity, experimental throughput, standardization, and long-term viability. Both precision-cut lung slices and airway explants preserve native tissue architecture and multicellular complexity but face constraints in culture duration, contamination risks, inter-sample variability, limited scalability, and donor availability (Klouda et al. 2021; Preuß et al. 2022; Marimoutou et al. 2024; Diodati et al. 2025). Organ-on-chip platforms, including the airway-chip system described here, enable controlled exposure conditions, quantitative barrier measurements, and parallel testing across multiple conditions. Selection of the most appropriate model, or combination of complementary models, depends on the specific scientific question, required endpoints, and experimental context to ensure suitability for mechanistic investigation and translational application.

As with all models, whether in vitro, ex vivo, or animal models, our airway-on-a-chip microphysiological system is not without limitations and challenges. A primary constraint is the absence of innate immune system components, limiting evaluation of inflammatory responses to early epithelial/endothelial signaling that would typically recruit neutrophils and macrophages. The lack of neutrophils and macrophages means key inflammatory amplification and resolution phases (phagocytosis, immune cell-mediated cytokine feedback) are modeled only indirectly. Inclusion of immune cells into this model would be expected to potentially amplify and extend the initial crisis phase, possibly manifesting at lower Cl_2 concentrations. For example, immune cell recruitment and activation following Cl_2-exposure might result in greater levels of oxidative stress, enhanced loss of cell viability, and delayed or prevented recovery of barrier function as measured by TEER. Such interactions warrant investigation in future iterations of this platform. We also note that airway-chip batches generated for each experimental dataset in this study utilized a single donor cell source, whereby data interpretation represents an approximation of population-level effects. Although single-source microphysiological system approaches have enabled critical advances in the field, including established alveolar (Huh et al. 2010), cardiac (Hoang et al. 2018), thymic (Montel-Hagen et al. 2019), gut (Kim et al. 2012), and multi-organ (Herland et al. 2020) model systems, future replication with additional demographically diverse donors will be necessary to establish generalizability across the population. Such validation studies would require substantial resources and may be limited to confirming key findings from developmental and discovery research, such as presented here. Given the magnitude of observed differences and low *P*-values for key findings in our study, we believe the interpretations within this study are informative approximations for such future studies. Finally, although our airway-chip model reproduces many characteristics of Cl_2 gas exposures documented in animal models, we observe tissue viability loss at lower Cl_2 concentrations compared with established lethal doses in animals. This difference may reflect our system's direct laminar flow exposure compared with animal models, where Cl_2 absorption varies by airway location (Nodelman and Ultman 1999). Additionally, anatomical differences between species (eg, rodents' larger relative nasal surface area) and experimental methods (tracheal intubation in large animals) affect Cl_2 delivery patterns. Despite these limitations, the strength of our model remains the range of possible exposure conditions with a set of chemical, biological, and physiological outcomes that model our current understanding of Cl_2 airway exposure impact, with the potential to gain new understanding of mechanisms and for testing MCMs.

The airway-on-a-chip microphysiological system overcomes several major challenges in the field and provides an opportunity to explore mechanistic and therapeutic questions in the future. Future developments include immune cell integration, utilization of donor cells representing relevant demographic characteristics such as sex, age, ethnicity, or disease state, and extended timepoint studies for recovery and fibrotic changes. Further validation against existing relevant animal models and expanded human donor datasets remains critical. The model's high throughput and cost-effectiveness facilitate MCM screening, allowing evaluation of hundreds of compounds for the cost of a single animal study. With the FDA Modernization Act 2.0, this platform could guide animal model selection and provide complementary data for therapeutic approvals, advancing the field's translational capabilities.

Acknowledgments

We would also like to acknowledge the support provided by the Proteomics and Metabolomics Shared Resource of the Wake Forest School of Medicine and Wake Forest Baptist Comprehensive Cancer Center, supported by the National Cancer Institute's Cancer Center Support Grant award number P30CA012197. Assistance from Jared A. Weis and Carlos Kengla for fluid/gas flow modeling, and computations performed using the Wake Forest University (WFU) High Performance Computing Facility, a centrally managed computational resource available to WFU researchers including faculty, staff, students, and collaborators.

Author contributions

S.V.M., T.D.S., A.J., and A.A. conceived and designed the study. S.V.M., S.A.P.R., Y.J., Y.Z., O.K., M.M., S.S., P.W.C., T.S.L., T.C.O., D.S., E.W., H.T., K.S., S.E.A., and A.R.H. developed and fabricated the airway-chip platform, exposure and microfluidic systems. K.L., T.Y., Y.Z., M.M., S.S., K.St., L.M., T.Si., G.K., F.C.M., S.So., and M.C.S. performed chemical/biological experimental procedures and data collection. T.Y., T.Si., J.C., L.A.C., G.L., C.C., T.E.R., S.J.W., and K.D.R. conducted RNA and transcriptomic analyses. Z.H., J.L., M.O., S.P., M.S.K., C.M.F., and A.C.B. conducted proteomic and metabolomic analysis. S.V.M., S.A.P.R., C.D.L., H.C.A., J.Z., A.Z., A.C.B., and K.D.R. performed data and bioinformatic analysis. S.V.M., L.A.C., M.O., F.C.M., S.So., S.J.W., C.M.F., M.C.S., and K.D.R. provided technical expertise and supervised specific aspects of the research. S.

V.M., K.D.R., and A.A wrote the manuscript with input from all authors. All authors reviewed and approved the final manuscript.

Supplementary material

Supplementary material is available at *Toxicological Sciences* online.

Funding

This project has been funded in whole or in part with Federal funds from the Department of Health and Human Services; Office of the Administration for Strategic Preparedness and Response; Biomedical Advanced Research and Development Authority, under Contract No. 75A50119C00058.

Conflicts of interest. None declared.

References

Ahmad S, Ahmad A, Hendry-Hofer TB, Loader JE, Claycomb WC, Mozziconacci O, Schoneich C, Reisdorph N, Powell RL, Chandler JD, *et al.* 2015. Sarcoendoplasmic reticulum Ca (2+) ATPase. A critical target in chlorine inhalation-induced cardiotoxicity. Am J Respir Cell Mol Biol. 52:492–502.

Alsafadi HN, Uhl FE, Pineda RH, Bailey KE, Rojas M, Wagner DE, Königshoff M. 2020. Applications and approaches for three-dimensional precision-cut lung slices: disease modeling and drug discovery. Am J Respir Cell Mol Biol. 62:681–691.

Amrani Y, Panettieri RA. 2002. Modulation of calcium homeostasis as a mechanism for altering smooth muscle responsiveness in asthma. Curr Opin Allergy Clin Immunol. 2:39–45.

Bader GD, Hogue CW. 2003. An automated method for finding molecular complexes in large protein interaction networks. BMC Bioinformatics. 4:2.

Baljinnyam T, Niimi Y, Salsbury JR, Fukuda S, Ouellette CM, Andersen CR, Hirasawa Y, Prough DA, Garner CE, Salzman AL, *et al.* 2023. Dose and gender dependence of chlorine inhalation in a conscious ovine model. Sci Rep. 13:22367.

Batchinsky AI, Martini DK, Jordan BS, Dick EJ, Fudge J, Baird CA, Hardin DE, Cancio LC. 2006. Acute respiratory distress syndrome secondary to inhalation of chlorine gas in sheep. J Trauma. 60:944–956.

Benam KH, Villenave R, Lucchesi C, Varone A, Hubeau C, Lee H-H, Alves SE, Salmon M, Ferrante TC, Weaver JC, *et al.* 2016. Small airway-on-a-chip enables analysis of human lung inflammation and drug responses in vitro. Nat Methods. 13:151–157.

Benjamini Y, Hochberg Y. 1995. Controlling the false discovery rate: a practical and powerful approach to multiple testing. J R Stat Soc. 57:289–300.

Blume C, Davies DE. 2013. In vitro and ex vivo models of human asthma. Eur J Pharm Biopharm. 84:394–400.

Boles SL, Pantazides BG, Perez JW, Sternberg MR, Crow BS, Blake TA. 2024. Establishing population values for chlorine exposure in the United States (2015–2016) using 2 chlorine biomarkers, 3-chlorotyrosine and 3, 5-dichlorotyrosine. J Appl Lab Med. 9:342–349.

Bosse GM. 1994. Nebulized sodium bicarbonate in the treatment of chlorine gas inhalation. J Toxicol Clin Toxicol. 32:233–241.

Carlisle M, Lam A, Svendsen ER, Aggarwal S, Matalon S. 2016. Chlorine-induced cardiopulmonary injury. Ann NY Acad Sci. 1374:159–167.

Clark GC, Elfsmark L, Armstrong S, Essex-Lopresti A, Gustafsson A, Ryan Y, Moore K, Paszkiewicz K, Green AC, Hiscox JA, *et al.* 2023. From "crisis to recovery": a complete insight into the mechanisms of chlorine injury in the lung. Life Sci. 312:121252.

Costa-Mattioli M, Walter P. 2020. The integrated stress response: from mechanism to disease. Science. 368:eaat5314.

Crow BS, Quinones-Gonzalez J, Pantazides BG, Perez JW, Winkeljohn WR, Garton JW, Thomas JD, Blake TA, Johnson RC. 2016. Simultaneous measurement of 3-chlorotyrosine and 3,5-dichlorotyrosine in whole blood, serum and plasma by isotope dilution HPLC-MS-MS. J Anal Toxicol. 40:264–271.

Das R, Blanc PD. 1993. Chlorine gas exposure and the lung: a review. Toxicol Ind Health. 9:439–455.

de Bruin-Hoegée M, van Damme IM, van Groningen T, Van der Riet-van Oeveren D, Noort D, van Asten AC. 2022. Elucidation of in vitro chlorinated tyrosine adducts in blood plasma as selective biomarkers of chlorine exposure. Chem Res Toxicol. 35:1070–1079.

Diodati NG, Qu G, Mehrad B, Schaller MA. 2025. Cryopreservation of human lung tissue for 3d ex vivo analysis. Respir Res. 26:187.

Elfsmark L, Ågren L, Akfur C, Bucht A, Jonasson S. 2018. 8-isoprostane is an early biomarker for oxidative stress in chlorine-induced acute lung injury. Toxicol Lett. 282:1–7.

Evans RB. 2005. Chlorine: state of the art. Lung. 183:151–167.

Fabregat A, Sidiropoulos K, Viteri G, Forner O, Marin-Garcia P, Arnau V, D'Eustachio P, Stein L, Hermjakob H. 2017. Reactome pathway analysis: a high-performance in-memory approach. BMC Bioinformatics. 18:142.

Ford DA, Honavar J, Albert CJ, Duerr MA, Oh JY, Doran S, Matalon S, Patel RP. 2016. Formation of chlorinated lipids post-chlorine gas exposure. J Lipid Res. 57:1529–1540.

González-Ruiz V, Pezzatti J, Roux A, Stoppini L, Boccard J, Rudaz S. 2017. Unravelling the effects of multiple experimental factors in metabolomics, analysis of human neural cells with hydrophilic interaction liquid chromatography hyphenated to high resolution mass spectrometry. J Chromatogr A. 1527:53–60.

Govier P, Coulson JM. 2018. Civilian exposure to chlorine gas: a systematic review. Toxicol Lett. 293:249–252.

Gustafson A, Elfsmark L, Karlsson T, Jonasson S. 2023. N-acetyl cysteine mitigates lung damage and inflammation after chlorine exposure in vivo and ex vivo. Toxicol Appl Pharmacol. 479:116714.

Hemstrom P, Jugg B, Watkins R, Jonasson S, Elfsmark L, Rutter S, Astot C, Linden P. 2024. Phospholipid chlorohydrins as chlorine exposure biomarkers in a large animal model. Toxicol Lett. 391:32–38.

Herland A, Maoz BM, Das D, Somayaji MR, Prantil-Baun R, Novak R, Cronce M, Huffstater T, Jeanty SSF, Ingram M, *et al.* 2020. Quantitative prediction of human pharmacokinetic responses to drugs via fluidically coupled vascularized organ chips. Nat Biomed Eng. 4:421–436.

Hirst S. 1996. Airway smooth muscle cell culture: application to studies of airway wall remodelling and phenotype plasticity in asthma. Eur Respir J. 9:808–820.

Hoang P, Wang J, Conklin BR, Healy KE, Ma Z. 2018. Generation of spatial-patterned early-developing cardiac organoids using human pluripotent stem cells. Nat Protoc. 13:723–737.

Honavar J, Samal AA, Bradley KM, Brandon A, Balanay J, Squadrito GL, MohanKumar K, Maheshwari A, Postlethwait EM, Matalon S, *et al.* 2011. Chlorine gas exposure causes systemic endothelial dysfunction by inhibiting endothelial nitric oxide synthase–dependent signaling. Am J Respir Cell Mol Biol. 45:419–425.

Huh D, Matthews BD, Mammoto A, Montoya-Zavala M, Hsin HY, Ingber DE. 2010. Reconstituting organ-level lung functions on a chip. Science. 328:1662–1668.

Humayun M, Chow C-W, Young EW. 2018. Microfluidic lung airway-on-a-chip with arrayable suspended gels for studying

epithelial and smooth muscle cell interactions. Lab Chip. 18:1298–1309.
Huynh Tuong A, Despreaux T, Loeb T, Salomon J, Megarbane B, Descatha A. 2019. Emergency management of chlorine gas exposure: a systematic review. Clin Toxicol. 57:77–98.
Jones R, Wills B, Kang C. 2010. Chlorine gas: an evolving hazardous material threat and unconventional weapon. West J Emerg Med. 11:151–156.
Kim HJ, Huh D, Hamilton G, Ingber DE. 2012. Human gut-on-a-chip inhabited by microbial flora that experiences intestinal peristalsis-like motions and flow. Lab Chip. 12:2165–2174.
Klouda T, Kim H, Kim J, Visner G, Yuan K. 2021. Precision cut lung slices as an efficient tool for ex vivo pulmonary vessel structure and contractility studies. J Vis Exp. 171:e62392.
Leach T, Gandhi U, Reeves KD, Stumpf K, Okuda K, Marini FC, Walker SJ, Boucher R, Chan J, Cox LA, *et al.* 2023. Development of a novel air-liquid interface airway tissue equivalent model for in vitro respiratory modeling studies. Sci Rep. 13:10137.
Lemiere C, Malo J, Boutet M. 1997. Reactive airways dysfunction syndrome due to chlorine: sequential bronchial biopsies and functional assessment. Eur Respir J. 10:241–244.
Leustik M, Doran S, Bracher A, Williams S, Squadrito GL, Schoeb TR, Postlethwait E, Matalon S. 2008. Mitigation of chlorine-induced lung injury by low-molecular-weight antioxidants. Am J Physiol Lung Cell Mol Physiol. 295:L733–L743.
Liu G, Betts C, Cunoosamy DM, Åberg PM, Hornberg JJ, Sivars KB, Cohen TS. 2019. Use of precision cut lung slices as a translational model for the study of lung biology. Respir Res. 20:162.
Liu MM, Liu JZ, Zhao CQ, Guo P, Wang Z, Wu H, Yu W, Liu R, Hai CX, Zhang XD. 2023. Protective effects of pentoxifylline against chlorine-induced acute lung injury in rats. BMC Pharmacol Toxicol. 24:12.
Marimoutou M, Patel V, Kim JH, Schaible N, Alvarez J, Hughes J, Obermok M, Rodriguez CI, Kallarakal T, Suki B, *et al.* 2024. The fibrotic phenotype of human precision-cut lung slices is maintained after cryopreservation. Toxics. 12:637.
Marsche G, Heller R, Fauler G, Kovacevic A, Nuszkowski A, Graier W, Sattler W, Malle E. 2004. 2-chlorohexadecanal derived from hypochlorite-modified high-density lipoprotein-associated plasmalogen is a natural inhibitor of endothelial nitric oxide biosynthesis. Arterioscler Thromb Vasc Biol. 24:2302–2306.
Martin JG, Campbell HR, Iijima H, Gautrin D, Malo JL, Eidelman DH, Hamid Q, Maghni K. 2003. Chlorine-induced injury to the airways in mice. Am J Respir Crit Care Med. 168:568–574.
Massa CB, Scott P, Abramova E, Gardner C, Laskin DL, Gow AJ. 2014. Acute chlorine gas exposure produces transient inflammation and a progressive alteration in surfactant composition with accompanying mechanical dysfunction. Toxicol Appl Pharmacol. 278:53–64.
Matalon S, Yu Z, Dubey S, Ahmad I, Stephens EM, Alishlash AS, Meyers A, Cossar D, Stewart D, Acosta EP, *et al.* 2024. Hemopexin reverses activation of lung eIF2α and decreases mitochondrial injury in chlorine-exposed mice. Am J Physiol Lung Cell Mol Physiol. 326:L440–L457.
Menaouar A, Anglade D, Baussand P, Pelloux A, Corboz M, Lantuejoul S, Benchetrit G, Grimbert F. 1997. Chlorine gas induced acute lung injury in isolated rabbit lung. Eur Respir J. 10:1100–1107.
Mo Y, Chen J, Humphrey DM, Jr Fodah RA, Warawa JM, Hoyle GW. 2015. Abnormal epithelial structure and chronic lung inflammation after repair of chlorine-induced airway injury. Am J Physiol Lung Cell Mol Physiol. 308:L168–L178.
Montel-Hagen A, Seet CS, Li S, Chick B, Zhu Y, Chang P, Tsai S, Sun V, Lopez S, Chen HC, *et al.* 2019. Organoid-induced differentiation of conventional T cells from human pluripotent stem cells. Cell Stem Cell. 24:376–389.e8.
Nishio T, Toukairin Y, Hoshi T, Arai T, Nogami M. 2021. Development of an LC-MS/MS method for quantification of 3-chloro-l-tyrosine as a candidate marker of chlorine poisoning. Leg Med (Tokyo). 53:101939.
Nodelman V, Ultman JS. 1999. Longitudinal distribution of chlorine absorption in human airways: a comparison to ozone absorption. J Appl Physiol (1985). 87:2073–2080.
Philippe R, Antigny F, Buscaglia P, Norez C, Becq F, Frieden M, Mignen O. 2015. Serca and PMCA pumps contribute to the deregulation of Ca2+ homeostasis in human CF epithelial cells. Biochim Biophys Acta. 1853:892–903.
Preuß EB, Schubert S, Werlein C, Stark H, Braubach P, Höfer A, Plucinski EKJ, Shah HR, Geffers R, Sewald K, *et al.* 2022. The challenge of long-term cultivation of human precision-cut lung slices. Am J Pathol. 192:239–253.
Rajan SAP, Aleman J, Wan M, Pourhabibi Zarandi N, Nzou G, Murphy S, Bishop CE, Sadri-Ardekani H, Shupe T, Atala A, *et al.* 2020. Probing prodrug metabolism and reciprocal toxicity with an integrated and humanized multi-tissue organ-on-a-chip platform. Acta Biomater. 106:124–135.
Robaszkiewicz A, Bartosz G, Soszynski M. 2011. Detection of 3-chlorinated tyrosine residues in human cells by flow cytometry. J Immunol Methods. 369:141–145.
Samal A, Honovar J, White CR, Patel RP. 2010. Potential for chlorine gas-induced injury in the extrapulmonary vasculature. Proc Am Thorac Soc. 7:290–293.
Samal AA, Honavar J, Brandon A, Bradley KM, Doran S, Liu Y, Dunaway C, Steele C, Postlethwait EM, Squadrito GL, *et al.* 2012. Administration of nitrite after chlorine gas exposure prevents lung injury: effect of administration modality. Free Radic Biol Med. 53:1431–1439.
Scenario 8: Chemical attack—chlorine tank explosion. 2004. Department of Homeland Security; [accessed February 9, 2024]. https://www.globalsecurity.org/security/library/report/2004/hsc-planning-scenarios-jul04_08.htm.
Si L, Bai H, Rodas M, Cao W, Oh CY, Jiang A, Moller R, Hoagland D, Oishi K, Horiuchi S, *et al.* 2021. A human-airway-on-a-chip for the rapid identification of candidate antiviral therapeutics and prophylactics. Nat Biomed Eng. 5:815–829.
Skardal A, Aleman J, Forsythe S, Rajan S, Murphy S, Devarasetty M, Pourhabibi Zarandi N, Nzou G, Wicks R, Sadri-Ardekani H, *et al.* 2020. Drug compound screening in single and integrated multi-organoid body-on-a-chip systems. Biofabrication. 12:025017.
Skardal A, Murphy SV, Devarasetty M, Mead I, Kang HW, Seol YJ, Shrike Zhang Y, Shin SR, Zhao L, Aleman J, *et al.* 2017. Multi-tissue interactions in an integrated three-tissue organ-on-a-chip platform. Sci Rep. 7:8837.
Sochaski MA, Jarabek AM, Murphy J, Andersen ME. 2008. 3-chlorotyrosine and 3,5-dichlorotyrosine as biomarkers of respiratory tract exposure to chlorine gas. J Anal Toxicol. 32:99–105.
Spickett CM. 2007. Chlorinated lipids and fatty acids: an emerging role in pathology. Pharmacol Ther. 115:400–409.
Szklarczyk D, Kirsch R, Koutrouli M, Nastou K, Mehryary F, Hachilif R, Gable AL, Fang T, Doncheva NT, Pyysalo S, *et al.* 2023. The string database in 2023: protein-protein association networks and functional enrichment analyses for any sequenced genome of interest. Nucleic Acids Res. 51:D638–D646.
Tang Y, Yu Y, Li R, Tao Z, Zhang L, Wang X, Qi X, Li Y, Meng T, Qu H, *et al.* 2023. Phenylalanine promotes alveolar macrophage

pyroptosis via the activation of CaSR in ARDS. Front Immunol. 14:1114129.

Tojo K, Tamada N, Nagamine Y, Yazawa T, Ota S, Goto T. 2018. Enhancement of glycolysis by inhibition of oxygen-sensing prolyl hydroxylases protects alveolar epithelial cells from acute lung injury. Faseb J. 32:2258–2268.

Van Sickle D, Wenck MA, Belflower A, Drociuk D, Ferdinands J, Holguin F, Svendsen E, Bretous L, Jankelevich S, Gibson JJ, *et al.* 2009. Acute health effects after exposure to chlorine gas released after a train derailment. Am J Emerg Med. 27:1–7.

Viswan A, Singh C, Rai RK, Azim A, Sinha N, Baronia AK. 2017. Metabolomics based predictive biomarker model of ARDS: a systemic measure of clinical hypoxemia. PLoS One. 12: e0187545.

Wang J, Winskog C, Edston E, Walther SM. 2005. Inhaled and intravenous corticosteroids both attenuate chlorine gas-induced lung injury in pigs. Acta Anaesthesiol Scand. 49:183–190.

Watkins R, Perrott R, Bate S, Auton P, Watts S, Stoll A, Rutter S, Jugg B. 2021. Development of chlorine-induced lung injury in the anesthetized, spontaneously breathing pig. Toxicol Mech Methods. 31:257–271.

White CW, Martin JG. 2010. Chlorine gas inhalation: human clinical evidence of toxicity and experience in animal models. Proc Am Thorac Soc. 7:257–263.

Xu J, Pan T, Qi X, Tan R, Wang X, Liu Z, Tao Z, Qu H, Zhang Y, Chen H, *et al.* 2020. Increased mortality of acute respiratory distress syndrome was associated with high levels of plasma phenylalanine. Respir Res. 21:99–13.

Zarogiannis SG, Jurkuvenaite A, Fernandez S, Doran SF, Yadav AK, Squadrito GL, Postlethwait EM, Bowen L, Matalon S. 2011. Ascorbate and deferoxamine administration after chlorine exposure decrease mortality and lung injury in mice. Am J Respir Cell Mol Biol. 45:386–392.

Zellner T, Eyer F. 2020. Choking agents and chlorine gas–history, pathophysiology, clinical effects and treatment. Toxicol Lett. 320:73–79.

Toxicological Sciences, 2025, 209, 1–15
https://doi.org/10.1093/toxsci/kfaf179
Research Article